Zeeman relaxation induced by spin-orbit coupling in cold antimony-helium collisions

Colin B. Connolly,[1,3] Yat Shan Au,[1,3] Eunmi Chae,[1,3] Timur V. Tscherbul,[3,4,5] Alexei A. Buchachenko,[6,7] Wolfgang Ketterle,[2,3] and John M. Doyle[1,3]

[1]*Department of Physics, Harvard University, Cambridge, Massachusetts 02138, USA*
[2]*Department of Physics, MIT, Cambridge, Massachusetts 02139, USA*
[3]*Harvard-MIT Center for Ultracold Atoms, Cambridge, Massachusetts 02138, USA*
[4]*Institute for Theoretical Atomic, Molecular, and Optical Physics, Harvard-Smithsonian Center for Astrophysics, Cambridge, Massachusetts 02138, USA*
[5]*Chemical Physics Theory Group, Department of Chemistry, University of Toronto, Toronto, Ontario M5S 3H6, Canada*
[6]*Department of Chemistry, M. V. Lomonosov Moscow State University, Moscow 119991, Russia*
[7]*Institute of Problems of Chemical Physics RAS, Chernogolovka, Moscow District 142432, Russia*

(Received 29 April 2013; published 15 July 2013)

We investigate Zeeman relaxation in cold Sb($^4S^\circ_{3/2}$)–He collisions in a magnetic field. Ensembles of $>10^{13}$ laser-ablated Sb atoms are cooled in cryogenic ^{4}He buffer gas to 800 mK and inelastic collisions are observed to equilibrate the m_J-state distribution to the translational temperature. The ratio γ of momentum transfer to inelastic collision rates is measured to be $\leqslant 9.1 \times 10^2$. We also perform quantum scattering calculations of Sb–^{4}He collisions, based on *ab initio* interaction potentials, that demonstrate significant anisotropy of the ground state induced by the spin-orbit interaction. Agreement is obtained between theory and experiment with a ≈10% increase in the *ab initio* potential depth. This work suggests that buffer-gas-cooled pnictogen atoms lighter than Sb can be loaded into a magnetic trap.

DOI: 10.1103/PhysRevA.88.012707 PACS number(s): 34.50.Cx, 34.20.Cf

I. INTRODUCTION

The study of inelastic collisions between atoms at low temperatures has expanded over the last decade to include a wide range of atomic systems exhibiting a range of atomic structures and interactions. Cold collisions of atoms with structureless rare gas targets, in particular, are a useful tool for studying anisotropy in the electron-density distribution (see Ref. [1] for a review). This anisotropy is explicit for atoms bearing nonzero orbital angular momentum L, such as atomic oxygen in the ^3P state, and may allow for strong, direct coupling between magnetic sublevels [2]. However, $L \neq 0$ is not a sufficient condition: anisotropy can be dramatically suppressed by spin-orbit coupling, like in the case of $^2P_{1/2}$ atoms [3,4], or by electron screening, like in the case of transition metals [5,6] and rare-earth-metal atoms [7,8] with the submerged open shells. Vice versa, multielectron S-state atoms may also exhibit anisotropic interactions due to internal couplings to excited anisotropic $L \neq 0$ states [9].

The pnictogens comprise an interesting test bed for observing an important and widespread interaction: spin-orbit coupling. All pnictogen atoms have the ground-state term $^4S^\circ_{3/2}$ arising from a half-filled p shell, although this term becomes less exact with increasing pnictogen mass. At the top of the column, nitrogen (N) is well described by this spherical term. Hence collisions of N with other atoms and with molecules are highly elastic, in many cases limited only by modest magnetic dipole-dipole interactions [10–12]. This collisional elasticity, along with fundamental importance to chemistry, has fueled interest in collisional physics with atomic N, including its use as a sympathetic coolant for molecule species. At the bottom of the pnictogen column is bismuth (Bi), the heaviest stable atom with a half-filled p shell. While nominally exhibiting the same electronic structure as N, Bi is affected by strong spin-orbit interactions that mix the anisotropy of excited states with the same electronic configuration into the otherwise spherical ground state. As a result, Bi exhibits highly inelastic collisions with helium [9] and is unlikely to be useful for sympathetic or evaporative cooling.

Anisotropy of an atom's interaction with a rare gas atom correlates to the anisotropy of the atom's response to a permanent external electric field (see Refs. [13–16]). A recent theoretical study [17] demonstrated that the anisotropic static dipole polarizability increases from N to Bi by 6 orders of magnitude, roughly in accord with the hydrogenlike Z^4 scaling of spin-orbit coupling with the nuclear charge Z. While the collision dynamics with a buffer gas have been explored for the extreme cases of N [18] and Bi [9], the transition between N-like elastic collisions and Bi-like inelasticity thus far has not. In addition, the measurements of cold Zeeman relaxation collisions (those that change the projection, m_J, of the atom's total angular momentum **J**) between N and Bi and helium provide only weak bounds on the inelastic collision rate that are orders of magnitude short of the theoretical predictions, leaving the experimental landscape rather sparse.

We report here a study of collisions between atomic antimony (Sb) and helium. As the second-heaviest pnictogen, Sb is well situated to probe the onset of relativistic effects. We directly measure the ratio γ of momentum transfer to inelastic collision rates and supplement it by the quantum scattering study based on the *ab initio* spin-orbit calculations. We find that the Sb–He system is strongly influenced by spin-orbit-induced anisotropy, but to an order of magnitude weaker extent than seen in Bi–He, consistent with the theoretical models and calculations. Zeeman relaxation driven by this anisotropy is too fast for straightforward magnetic trapping of Sb atoms using buffer-gas cooling. Our results suggest, however, that such trapping could be achieved for the lighter and more isotropic [17] pnictogens arsenic (As) and phosphorus (P).

II. EXPERIMENT

To measure the rate of spin relaxation in Sb–He collisions, we prepare a buffer-gas-cooled sample of Sb atoms in a magnetic field and observe decay from the low-field-seeking (LFS) stretched state ($m_J = J = 3/2$) to lower-energy high-field seeking (HFS) states. The experiment takes place inside a double-walled G-10 CR fiberglass-epoxy composite cell. Superfluid helium fills the space between the two walls to surround the cell and maintain a uniform temperature over its length. A superfluid helium link anchors the cell to a dilution refrigerator to maintain a cell temperature of 800 mK. ^{4}He buffer gas is added and removed via a small impedance to a separate cold gas reservoir to achieve a variable gas density that remains effectively constant for the duration of a single measurement (<1 s). The cell sits inside the bore of a pair of superconducting Helmholtz magnetic field coils.

We produce $>10^{13}$ cold Sb atoms by ablating a solid Sb metal target into the buffer gas. The atoms are produced in an equal distribution across all electronic and nuclear spin states of the ground $^4S^\circ_{3/2}$ manifold. After cooling to the cell temperature, the Sb atoms diffuse to the cell walls and stick there, undergoing 10^4–10^5 collisions with the helium buffer gas. The magnetic field is uniform over most of the cell and does not significantly affect the diffusive transport.

We probe the atomic Sb ensemble by laser absorption on the $^4S^\circ_{3/2} \rightarrow {}^4P_{5/2}$ transition at 206.9 nm. The probe light is generated by single harmonic generation (SHG) in a beta barium borate (BBO) crystal using a resonant cavity. Approximately 80 mW of light from an injection-locked diode laser at the 413.8-nm fundamental wavelength results in ≈100 nW of UV. We note that the doubling cavity lock is not optimized and an order of magnitude greater SHG conversion efficiency is likely possible with the same input power in this system. The UV beam is split into an intensity reference beam and a probe beam that enters the cryogenic dewar and retroreflects from a mirror in the cell. Dielectric mirrors mounted in long tubes provide spectral and spatial filtering of unwanted light, after which both beams are incident upon photomultiplier tubes.

The hyperfine spectrum of the $^4S^\circ_{3/2} \rightarrow {}^4P_{5/2}$ transition at 206.9 nm spans 30 GHz; we are unable to scan our laser across the entire spectrum within the diffusion time. Instead, we hold the laser frequency constant, resonant with a transition from either the stretched LFS or HFS states ($m_J = \pm J$), and monitor the optical depth (OD) over time. The two transitions used are closely spaced in frequency with opposite Zeeman shifts, allowing one or the other to be tuned to resonance with ≈10% adjustment of the magnetic field. The ^{4}He density in the cell decays over tens of minutes, during which we alternate between measurements of the LFS and HFS state decay, at approximately 1-min intervals. An example pair of such measurements is shown in Fig. 1. Immediately following translational cooling in the buffer gas, the relative LFS and HFS state populations come to thermal equilibrium through inelastic Sb–^{4}He collisions. Indeed, we initially observe rapid LFS decay and a corresponding increase in the HFS population. Once in equilibrium, the two states decay in tandem due to diffusion to the cell walls. From the HFS data at late times, we use this diffusive decay to determine the Sb–^{4}He collision rate. Interpolating between HFS state decay measurements provides the collision rate at the times at which LFS state measurements are made.

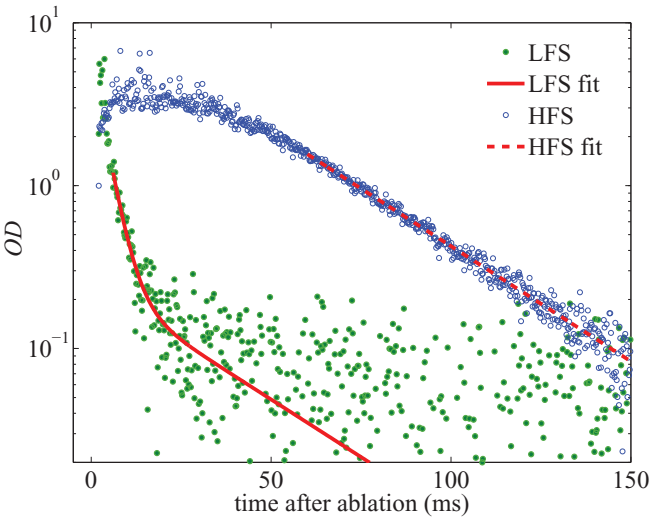

FIG. 1. (Color online) Decay of low- and high-field seeking (LFS and HFS) states ($m_J = +3/2$ and $-3/2$) of Sb at $T = 800$ mK and $B = 0.86$ T.

III. DECAY MODEL

We describe here a simplified version of the relaxation model developed in Ref. [19]. For a gas of Sb atoms with equal m_J state populations, we expect the time evolution of the $m_J = J$ state to be driven by a combination of diffusion in the buffer gas and Zeeman relaxation to states of lower m_J. The lowest-order diffusion mode decays exponentially with time constant τ_d, given by [20]

$$\tau_\mathrm{d} = \frac{n_\mathrm{b}\sigma_\mathrm{d}}{\bar{v}G}, \tag{1}$$

$$G = \frac{3\pi}{32}\left(\frac{j_{01}^2}{r^2} + \frac{\pi^2}{L^2}\right), \tag{2}$$

in a cylindrical cell of radius r and length L, where n_b is the buffer gas density, σ_d is the thermally averaged momentum transfer cross section, $\bar{v} = (8k_\mathrm{B}T/\pi\mu)^{1/2}$ is the mean Sb–^{4}He collision velocity at temperature T with reduced mass μ, and $j_{01} \approx 2.405$ is the first root of the Bessel function $J_0(x)$. Higher-order diffusion modes decay much more rapidly and can be ignored at late times.

As an Sb atom diffuses through the buffer gas, an inelastic collision with ^{4}He can cause a transition to a state of different m_J. For the stretched LFS state with $m_J = J$, this transition only occurs to states of lower m_J, which is energetically favorable. The time constant for this process, τ_R, is found by including all possible spin relaxation transitions:

$$\tau_\mathrm{R} = (n_\mathrm{b}\, k_\mathrm{R})^{-1}, \tag{3}$$

$$k_\mathrm{R} = \sum_{m'_J \neq J} k_{m_J \rightarrow m'_J}, \tag{4}$$

where k_R is the total Zeeman relaxation rate constant. At zero temperature, the low-field-seeking state decays

exponentially under the combined effect of diffusion and relaxation. However, at finite temperature there are two important modifications to the time dependence.

First, atoms with $m_J < J$ will also experience m_J-changing collisions, and the collision energy will sometimes be sufficient to promote an atom to a state of higher m_J, thus repopulating the stretched state [19]. These thermal excitations will alter the relaxation to equilibrium, an effect that is amplified at higher temperatures and in atoms with large J and thus small sublevel splitting. We have numerically modeled this effect for our experimental conditions and we find that it leads to a $<10\%$ underestimation of k_R.

Second, at finite temperature there will remain a thermal population in the $m_J = J$ state, even at equilibrium. Thus the time dependence of this state's population N_J, neglecting thermal excitations, will be

$$N_J(t) = \tilde{N} e^{-t/\tau_d}\left[f_{eq} + \left(\frac{1}{2J+1} - f_{eq}\right)e^{-t/\tau_R}\right], \quad (5)$$

where $\tilde{N}$ is the total initial atom population,

$$f_{eq} = \frac{\exp\left[-\frac{g_J J \mu_B B}{k_B T}\right]}{\sum_{m_J} \exp\left[-\frac{g_J m_J \mu_B B}{k_B T}\right]} \quad (6)$$

is the thermal equilibrium fraction of the total population in the $m_J = J$ state at temperature T and magnetic field B, k_B is the Boltzmann constant, and g_J is the Landé g factor. Note that at zero temperature, $f_{eq} \to 0$ and Eq. (5) simplifies to the appropriate simple exponential.

The elasticity of the colliding system is described by the dimensionless ratio $\gamma = k_d/k_R$ of the elastic and inelastic collision rates, where $k_d = \sigma_d \bar{v}$. Large values of γ imply that many collisions can occur before a m_J-changing transition occurs. We can compute γ directly from Eqs. (1) and (3) to yield

$$\gamma = \bar{v}^2 G \tau_d \tau_R. \quad (7)$$

While it is in principle possible to extract γ from a single measurement, we make many measurements over a range of ^{4}He densities (i.e., a range of τ_d) and compare the results to the form of Eq. (7), which predicts $\tau_R \propto \tau_d^{-1}$ at constant γ. This provides a check against systematic error. In particular, there may be other processes affecting the decay of the LFS state or of all states—such as molecule formation [21] or temperature variation—which exhibit a different dependence on buffer gas density.

IV. RESULTS AND ANALYSIS

We fit the HFS decay at late times to exponential decay to extract the diffusion time τ_d and fit the LFS decay to Eq. (5) to extract τ_R (Fig. 1). The LFS data are fit on the interval after $t = 6$ ms to allow for decay of higher-order diffusion modes and of unwanted fluorescence in the cell caused by ablation. To reduce statistical uncertainty and minimize systematic error, we constrain the LFS fit by fixing the value of τ_d to be the same as that of the HFS state. Since only one state is monitored during any single measurement, all values of τ_d determined from HFS measurements are first fit to the exponential decay expected due to buffer gas being slowly pumped (over tens of minutes) back through the filling impedance. The fitted function for the exponential decay of τ_d is evaluated at the times when LFS measurements are made to fix τ_d, in turn, for fitting the LFS state decay using Eq. (5). In addition, we constrain f_{eq} to its minimum χ^2 value across all measurements made at the same temperature and magnetic field, since f_{eq} is not a function of buffer gas density.

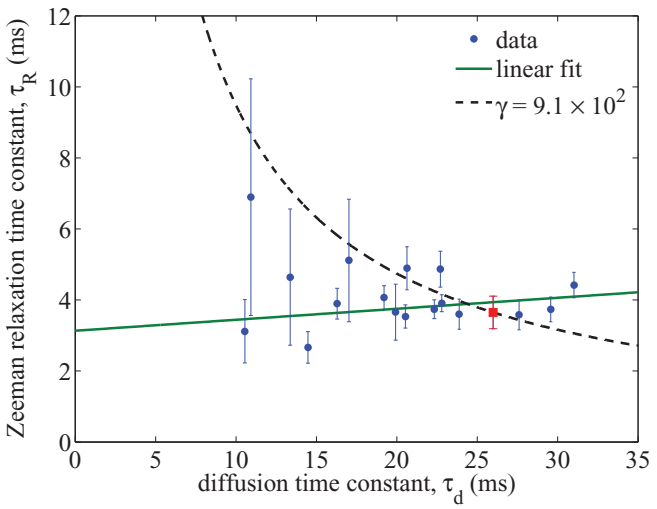

FIG. 2. (Color online) Apparent Zeeman relaxation time constant τ_R obtained from fitting low-field-seeking (LFS) state decay at $T = 800$ mK and $B = 0.86$ T to Eq. (5). The data do not follow the functional form of Zeeman relaxation predicted by Eq. (7) (dashed black line), and a linear fit (solid green line) yields a slope statistically consistent with zero. Hence the LFS state decay is likely modified by cooling of the cell and is thus slower than the actual Zeeman relaxation rate. The red square point is used to set a bound of $\gamma \leqslant 9.1 \times 10^2$ (dashed black line); data with lower τ_d may be affected by a transient increase in buffer gas density caused by ablation.

The fitting results are plotted in Fig. 2. There is no statistically significant dependence of the apparent relaxation time on buffer gas density. Therefore the decay of the LFS state is not a direct observation of the Zeeman relaxation rate. Instead, the decay is most likely a combination of Zeeman relaxation and cooling of the cell and buffer gas after heating caused by ablation. The reason for this is as follows: if the cell temperature is not stable on the time scale of the decay, then the form of the decay predicted by Eq. (5) will be modified by the temperature dependence of f_{eq} (and to a lesser extent, that of τ_d). In the limit of extremely rapid relaxation ($\tau_R \to 0$), the magnetic sublevel distribution will be in equilibrium with the translational temperature, and the LFS state decay will closely follow the cell's cooling profile. Since we do not have sufficient knowledge of the temporal and spatial thermal profile of the cell and buffer gas to separate translational cooling from Zeeman relaxation, the experiment is only able to bound the relaxation rate as being at least as fast as the observed equilibration.

We set an upper bound on the collision ratio γ using Eq. (7) and the data with the shortest value of the product $\tau_d \times \tau_R$. In doing so, we consider only data for which $\tau_d > 25$ ms, for which the absorption signal strength and lifetime are large enough to allow for confirmation that the buffer gas density is constant over the fitting interval. To be conservative, we do not

use data with shorter diffusion times because of the possibility that a short-lived pulse of helium desorbed from the cell walls by the ablation pulse could cause the early-time buffer gas density to differ from the late-time density where τ_d is measured—such a discrepancy could cause an underestimation of γ. At higher buffer gas densities, the effect of this pulse is negligible. The best constraint on γ is therefore obtained from the red (square) point in Fig. 2, which yields $\gamma \leqslant 9.1 \times 10^2$.

V. ELECTRONIC STRUCTURE

In this section, we investigate the electronic structure of the Sb–He complex that determines collision dynamics. We consider the states of the complex correlating to the three lowest asymptotic limits that corresponds to the $^4S^\circ$, $^2D^\circ$, and $^2P^\circ$ terms (given as $^{2S+1}L^p$) of the Sb($5s^2 5p^3$) atom. In the standard LS coupling notation, $^{2S+1}\Lambda^\sigma$, these are $^4\Sigma^-(^4S^\circ)$, $^2\Delta(^2D^\circ)$, $^2\Pi(^2D^\circ)$, $^2\Sigma^-(^2D^\circ)$, $^2\Pi(^2P^\circ)$, and $^2\Sigma^+(^2P^\circ)$. Here S is the total electronic spin angular momentum, L is the total electronic angular momentum of an atom, Λ is the projection of $\hat{L}$ onto the interatomic axis $\mathbf{R}$, and p and σ designate the parities of the electronic wave functions.

The LS potential energy curves are computed in the scalar-relativistic approximation within the internally contracted multireference configuration interaction (MRCI) method [22]. MRCI, as well as the preceding state-averaged complete active space multiconfigurational self-consistent field (CASSCF) [23,24], distributes seven electrons over the five active orbitals representing the $5s5p$ shells of Sb and the $1s$ shell of He. For the Sb atom, we employ the small-core (28-electron) relativistic effective core potential ECP28MDF by Metz *et al.* [25] together with the corresponding augmented quintuple-ζ correlation-consistent polarized valence (aug-cc-pV5Z) basis set [26]. For the He atom, we adopt an equivalent aug-cc-pV5Z set [27].

To provide better description of the ground $^4\Sigma^-$ electronic state, we also compute its potential energy curve using the coupled cluster method with single, double, and noniterative triple excitations, CCSD(T) [28,29], with the standard counterpoise correction to the basis set superposition error [30]. To saturate the dominant dispersion contributions to interaction energy, the $3s3p2d2f1g$ set of the bond functions [31] is added to the atom-centered basis set described above at the midpoint of the Sb–He interatomic distance R.

The MRCI excitation energies are added to the CCSD(T) ground-state potential energy curve and shifted in energy to reproduce the experimental centers of the $^2P^\circ$ and $^2D^\circ$ fine-structure multiplets [32] E_P and E_D at large (50 Å) internuclear distance.

Since the energy splittings between the states correlating to the asymptotes with different L are much larger than weak atom-atom interaction, the differential radial and angular nonadiabatic couplings are neglected.

Vectorial spin-orbit (SO) interaction is treated using the full Breit-Pauli SO operator at the CASSCF level of theory. The full SO matrix spanned by all 23 components of the six LS states is obtained and used to extract five independent SO coupling matrix elements, defined as in Ref. [9], after its transformation to the pure $|LM_LSM_S\rangle$ angular momentum representation. In the limit of separated atoms, A_D and A_P elements are related to the internal splittings of isolated $^2D^\circ$ and $^2P^\circ$ multiplets, respectively, whereas B_{SP} and B_{PD} describe the couplings between states of $^4S^\circ$ and $^2P^\circ$ multiplets and between those of $^2P^\circ$ and $^2D^\circ$ multiplets, respectively. The $^4S^\circ$ and $^2D^\circ$ terms do not interact with each other in an atom, but interaction with He induces the SO coupling between the ground $^4\Sigma^-$ and $^2\Pi(^2D^\circ)$ states, B_{SD}.

TABLE I. *Ab initio* parameters describing SO energy levels of Sb and Bi atoms (cm^{-1}).

Parameter	E_D	E_P	B_{SP}	B_{PD}	A_D	A_P
Sb, this work	9224	16 047	2747	3081	73	14
Bi [9]	8944	15 769	8610	9637	92	131

Diagonalization of the electronic Hamiltonian matrix at the separated atom limit gives the following energies for the fine-structure atomic levels (relative to the $^4S^\circ_{3/2}$ level in cm^{-1}, with experimental values [32] in parentheses): $^2D^\circ_{3/2}$ 8731 (8512), $^2D^\circ_{5/2}$ 9636 (9854), $^2P^\circ_{1/2}$ 16 546 (16 395), and $^2P^\circ_{3/2}$ 18 100 (18 464). The deviations do not exceed 400 cm^{-1} and are generally smaller than are found in the Bi–He calculations [9]. Table I compares the asymptotic parameters obtained here for Sb–He with those computed for Bi–He in Ref. [9]. It is evident that while the Coulomb excitation energies vary from Bi to Sb insignificantly, the SO matrix elements decrease dramatically; the dominant intermultiplet couplings B_{SP} and B_{PD} both decrease by a factor of 3.12.

Scalar-relativistic CCSD(T) calculations reveal that Sb–He forms a van der Waals complex bound predominantly by the dispersion interaction. The ground-state interaction energy D_e is determined to be 11.1 cm^{-1} at the equilibrium distance $R_e = 4.50$ Å, which implies slightly stronger binding than that of the the Bi–He complex ($D_e = 10.0\ cm^{-1}$, $R_e = 4.64$ Å [9]), despite a weaker dispersion interaction (the leading dispersion coefficient C_6 is equal to 23.6 atomic units (a.u.), while for Bi–He $C_6 = 25.6$ a.u.). The reason for this is the shorter range of the repulsive exchange interaction.

Excited scalar-relativistic potentials are also similar for the two systems. In particular, the $^2\Pi$ and $^2\Sigma^+$ states of Sb–He correlating to the $^2P^\circ$ atomic term have $D_e = 7.5\ cm^{-1}$, $R_e = 4.83$ Å and $D_e = 11.0\ cm^{-1}$, $R_e = 4.53$ Å, respectively ($D_e = 6.9\ cm^{-1}$, $R_e = 4.96$ Å and $D_e = 11.5\ cm^{-1}$, $R_e = 4.44$ Å for Bi–He [9]). This indicates that the anisotropy of the $^2P^\circ$ state is slightly larger for the Bi atom, in accord with the behavior of static dipole polarizabilities [17]. Similarity of the potential energy curves of all the molecular states arising from the ns^2np^3 configuration of Sb or Bi likely reflects the similarity in the scalar dipole polarizabilities of the corresponding atomic states.

The SO interaction does not affect the ground $^4\Sigma^-$ state to the first order of perturbation theory. At higher orders, however, SO couples the ground state with the excited $^2\Lambda$ states split by the interaction anisotropy. As a result, the degeneracy of the $\Omega = 3/2$ and $1/2$ components of the ground state is lifted, as shown in Fig. 3. [Ω is the projection of the total (orbital plus spin) electronic angular momentum onto the interatomic axis.] As shown in Ref. [17], this is the source of anisotropy in the static dipole polarizability of $^4S^\circ$ states of the pnictogens.

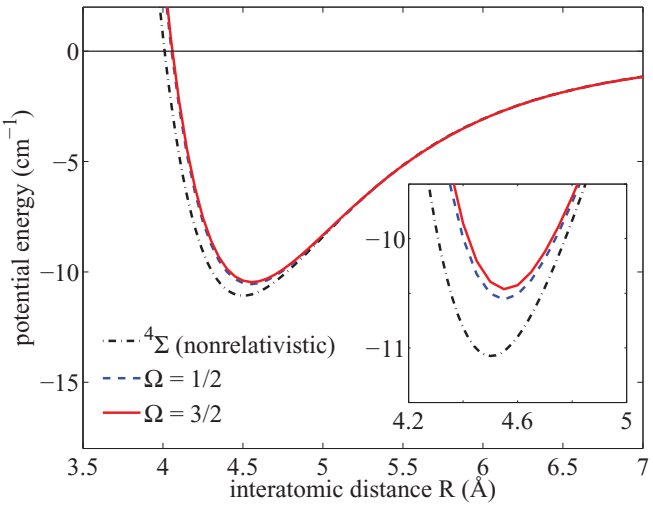

FIG. 3. (Color online) Sb–He interaction potentials of the lowest-energy non-relativistic and SO-coupled states. The inset enlarges the region near the potential minima.

To the second order of perturbation theory, only the coupling to the excited $^2\Pi(^2P^\circ)$ and $^2\Sigma^+(^2P^\circ)$ states given by the B_{SP} parameter contributes to the splitting. The same conclusion was inferred from the analysis of Bi–He interactions [9], which found that the splitting ΔE_Σ between the $\Omega = 3/2$ and $1/2$ SO components of the ground state (i.e., the interaction anisotropy) can be approximated to second order as [9]

$$\Delta E_\Sigma = \frac{2}{3}\left[\frac{B_{SP}(R)}{E_P}\right]^2 [V_{P\Pi}(R) - V_{P\Sigma}(R)], \tag{8}$$

where $V_{P\Pi}$ and $V_{P\Sigma}$ are the potential energy curves of the excited $^2\Pi$ and $^2\Sigma^+$ states, respectively. Figure 4 shows that Eq. (8) closely reproduces the results of numerical diagonalization of the *ab initio* coupling matrices for both the Sb–He and Bi–He systems. Comparing *ab initio* results for the two systems indicates that each of the factors in Eq. (8)—the energy and anisotropy of the $^2P^\circ$ state and its SO coupling to the ground state—vary with increasing pnictogen mass such

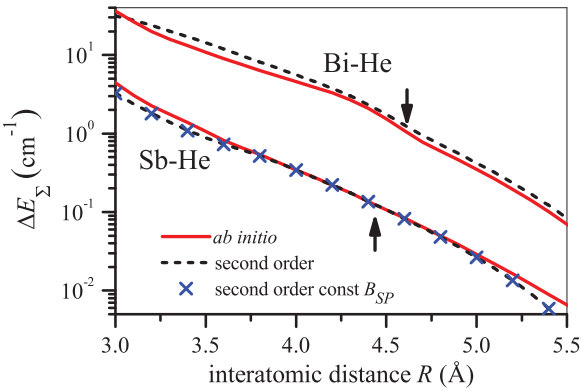

FIG. 4. (Color online) Radial dependence of the splittings between the $\Omega = 1/2$ and $\Omega = 3/2$ adiabatic potential energy curves of the ground $^4\Sigma^-$ states of the Sb–He and Bi–He systems. The *ab initio* results are well approximated by the second-order expression [Eq. (8)], even if the B_{SP} parameter is approximated by its asymptotic constant value. Arrows indicate the ground-state equilibrium distance.

that interaction anisotropy is increased, although the coupling B_{SP} plays by far the dominant role. It should also be noted that B_{SP} varies with R very weakly, so that the ground-state splitting is perfectly reproduced with the asymptotic B_{SP} value. The A_P and B_{SD} SO couplings show more pronounced dependence on R but affect the ground state only in the third and fourth orders of perturbation theory. In accord with this reasoning, the effect of their radial dependence on Bi–He collision dynamics was found to be small [9].

VI. SCATTERING CALCULATIONS

In order to interpret our measurement and draw comparisons to other pnictogen systems, we performed rigorous quantum scattering calculations [2] based on the *ab initio* interaction potentials and matrix elements presented in the previous section. Our theoretical approach closely resembles that implemented before for the Bi–He system in Ref. [9]. The Sb–He interaction Hamiltonian is written in atomic units as [9]

$$\hat{H} = -\frac{1}{2\mu R}\frac{\partial^2}{\partial R^2}R + \frac{\hat{\ell}^2}{2\mu R^2} + \hat{V}(R) + \hat{H}_{\rm as}, \tag{9}$$

where μ is the reduced mass and $\hat{\ell}$ is the rotational angular momentum of the nuclei. The asymptotic Hamiltonian describing the electrostatic, SO, and external field-induced interactions in the isolated Sb atom is given by

$$\hat{H}_{\rm as} = \hat{H}_{\rm SI} + \hat{H}_{\rm SO} + \hat{H}_B, \tag{10}$$

where

$$\hat{H}_{\rm SI} = \sum_{L,L'} H_{\rm SI}^{LL'}|L\rangle\langle L'| \tag{11}$$

accumulates the terms of the electronic Hamiltonian of the free atom that do not depend explicitly on the spin. Its diagonal matrix elements $H_{\rm SI}^{LL}$, with $L = 0,1$, and 2, are the electronic excitation energies E_S, E_P, and E_D, respectively, with $E_S = 0$. Nondiagonal matrix elements correspond to the interstate couplings, $H_{\rm SI}^{01} = B_{SP}$ and $H_{\rm SI}^{12} = B_{PD}$. The remaining diagonal part of the SO interaction is described by the SO Hamiltonian,

$$\hat{H}_{\rm SO} = \sum_{LS} \hat{H}_{\rm SO}^{LS}|LS\rangle\langle LS|, \tag{12}$$

for which we use the mean-field approximation,

$$\hat{H}_{\rm SO}^{LS} = A_L \hat{L}\cdot\hat{S}, \tag{13}$$

justified by the weakness of intramultiplet SO couplings A_P ($L = 1$) and A_D ($L = 2$) as compared with the splittings between the different LS states (Table I). The use of R-independent asymptotic values of the coupling terms is justified in the previous section. The Hamiltonian $\hat{H}_B$ describes the interaction of the atom with an external magnetic field of strength B and is given by Eq. (5) of Ref. [9].

The Sb–He interaction potential operator in Eq. (9) is given by

$$\hat{V}(\mathbf{R},\mathbf{r}) = \sum_{L,L'} \hat{V}^{LL'}(R)|L\rangle\langle L'|. \tag{14}$$

The diagonal part of the operator

$$\hat{V}^{LL} = \sum_{\mu} V_\mu^{LL}(R) P_\mu(\mathbf{R}\cdot\mathbf{r}), \tag{15}$$

where P_μ is a Legendre polynomial [2], describes the interaction of an atom in a state with orbital angular momentum L with a structureless atom. The off-diagonal part ($V^{LL'}$ with $L' \neq L$) describes the coupling induced by the interatomic interaction between states of different L. The matrix elements of Eq. (14) in the direct-product scattering basis $|(LS)Jm_J\rangle|lm_l\rangle$ are given by

$$\begin{aligned}
&\langle (LS)Jm_J|\langle \ell m_\ell|\hat{V}(\mathbf{R},\mathbf{r})|(L'S')J'm'_J\rangle|\ell' m'_\ell\rangle \\
&\quad = \delta_{SS'}(-1)^{L+S+J'+J-m_J-m'_\ell}[(2L+1)(2L'+1) \\
&\qquad \times (2J+1)(2J'+1)(2\ell+1)(2\ell'+1)]^{1/2} \\
&\qquad \times \sum_\lambda V_\lambda^{LL'}(R) \begin{Bmatrix} L & J & S \\ J' & L' & \lambda \end{Bmatrix} \\
&\qquad \times \begin{pmatrix} J & \lambda & J' \\ -m_J & m_J - m'_J & m'_J \end{pmatrix} \begin{pmatrix} \ell & \lambda & \ell' \\ -m_\ell & m_\ell - m'_\ell & m'_\ell \end{pmatrix} \\
&\qquad \times \begin{pmatrix} L & \lambda & L' \\ 0 & 0 & 0 \end{pmatrix} \begin{pmatrix} \ell & \lambda & \ell' \\ 0 & 0 & 0 \end{pmatrix}, \qquad (16)
\end{aligned}$$

where the symbols in figure brackets and parentheses are 3-j and 6-j symbols, respectively. This expression generalizes Eq. (3) of Ref. [3] to collision-induced transitions between the different L states.

The details of scattering calculations have been presented elsewhere [9]. In brief, the wave function of the Sb–He collision complex is expanded in a direct-product basis set (Eq. (16) here and Eq. (2) of Ref. [9]), and the radial expansion coefficients were obtained by solving the coupled differential equations given by Eq. (4) of Ref. [9]. The scattering basis included the $|(LS)Jm_J\rangle$ states of Sb with $L = 0$, 1, and 2 (S, P, and D states) [9] augmented with seven partial waves ($\ell = 0$–6). The coupled equations were integrated on a grid of $R \in [1,100]$ Å with a grid spacing of 0.02 Bohr radii using the scattering code developed previously for Bi–He by Krems [9]. Scattering calculations were performed at 200 collision energies between 0.02 and 4 cm^{-1} with a constant step size of 0.02 cm^{-1}.

For accurate comparison with the experiment, we first calculate the momentum transfer cross section by solving a one-dimensional (1D) scattering problem based on the lowest non-relativistic Sb–He potential of $^4\Sigma^-$ symmetry (Fig. 3). To validate this approach, we also compute the total elastic cross section in the same manner and compare it to the exact multichannel result (Fig. 5). We find that the 1D approximation reproduces the exact cross section to within 10% over the temperature range 0.1–2 K, including scattering resonances.

Second, we compute the quantum scattering cross section for transitions from the $m_J = J = 3/2$ stretched Zeeman state to all final m_J states. The rate coefficients for momentum transfer and Zeeman relaxation are calculated from the cross sections by thermally averaging over the Maxwell-Boltzmann distribution. The total Zeeman relaxation rate k_R is calculated by adding contributions for transitions to all other magnetic sublevels [Eq. (4)]. The calculated ratio γ of the two rates is shown in Fig. 6 for several values of the magnetic field B, along with the bound obtained by the experiment at $B = 0.86$ T. We find that the calculated value exceeds the experimental upper bound by about a factor of 2.

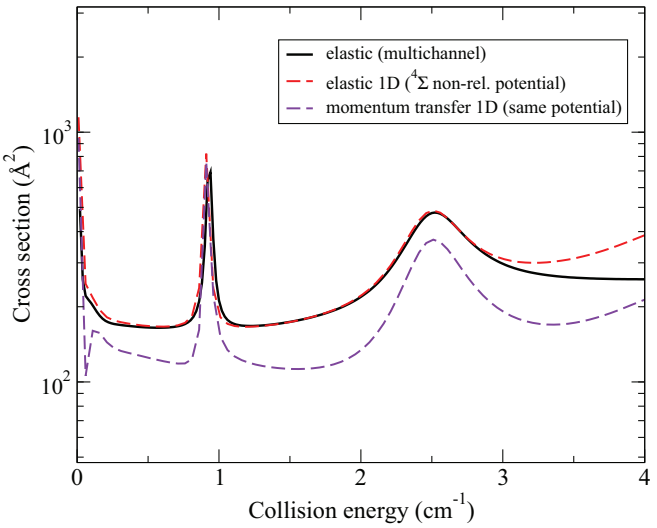

FIG. 5. (Color online) Calculated Sb-^{4}He total elastic and momentum transfer cross sections. The solid curve is an exact multichannel calculation and the dashed curves are calculated using a 1D approximation that includes only the lowest non-relativistic adiabatic potential. The excellent agreement between the two calculations of the total elastic cross section (solid black and dashed red curves) implies that the approximation is good over this temperature range.

Since the inaccuracy in interaction potentials is the most important factor affecting γ, we repeat our calculation with all the scalar-relativistic interaction potentials [$V_\mu^{LL}(R)$ in Eq. (15)] scaled by a constant factor λ (Fig. 7). We find that γ decreases nearly monotonically over this range and that theory and experiment are in agreement for a deepening of the potentials by ≈10%. This level of error is reasonable for the *ab initio* calculations, which are expected to slightly underestimate the attractive dispersion interaction due to the finite basis set and included correlations.

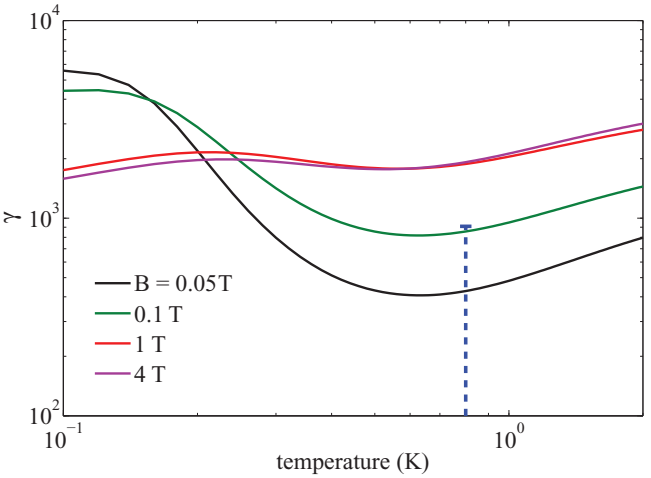

FIG. 6. (Color online) Calculated Sb-^{4}He momentum-transfer-to-inelastic collision rate ratio γ. The experimental upper bound obtained at $B = 0.86$ T is also shown (dashed blue line).

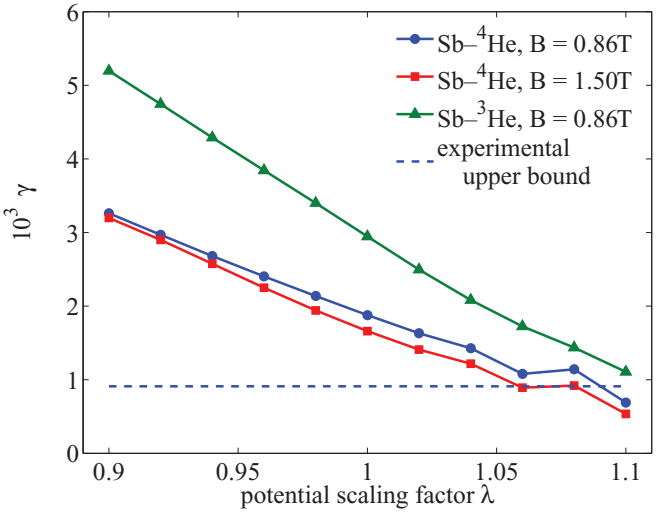

FIG. 7. (Color online) Calculated momentum-transfer-to-inelastic collision rate ratio γ as a function of the interaction potential scaling factor λ. The blue circles are those corresponding to the experimental parameters. The experimental bound (dashed line) is in agreement with theory for $\lambda = 1.1$. Also shown are calculated results for the Sb–^{3}He system (green triangles), for which the inelasticity is reduced due the absence of a collision resonance near 1 K.

In comparison to the Bi–He system under similar conditions [9], the rate of Zeeman relaxation in Sb–He collisions is an order of magnitude lower, due to the weaker SO coupling of the ground $^4S^\circ_{3/2}$ state to anisotropic states. This is in agreement with the reduction in the interaction anisotropy ΔE_Σ (Fig. 4), as well as with a Z^4 scaling.

VII. CONCLUSION

We present experimental and theoretical results for Sb–He collisions that demonstrate significant distortion of the isotropic $^4S^\circ_{3/2}$ ground state due to the SO interaction. The resulting electronic interaction anisotropy drives rapid Zeeman relaxation in this system. However, we show theoretically that relaxation occurs at a rate about an order of magnitude slower than the Bi–He system, in agreement with the second-order SO approximation [Eq. (8)] developed in Ref. [9]. This is also consistent with the strong relativistic dependence on Z of the SO interaction. Our measurement at $T = 800$ mK and $B = 0.86$ T confirms the strong inelasticity, setting a bound on the momentum-transfer-to-inelastic collision rate ratio of $\gamma \leqslant 9.1 \times 10^2$. This bound implies that the *ab initio* potential underestimates the interaction strength by $\approx$10%, which provides valuable feedback to the theoretical models.

The rapid Sb–He Zeeman relaxation that we observe here precludes buffer-gas loading of Sb into a magnetic trap. The rates of Zeeman relaxation of Bi, Sb, and N in collisions with He are consistent with a Z^4 scaling for temperatures near 1 K and magnetic fields near 1 T [9,18], following the same trend shown in the static dipole polarizability anisotropy [17]. A natural extension of this work is to look further up the pnictogen column to arsenic (As) and phosphorus (P), for which our theoretical model predicts significantly reduced relaxation in collisions with He. We can estimate these rates using Eq. (8) and the energies and SO coupling parameters of the isolated atoms [17,32]. Assuming conservatively that the difference $V_{P\Pi} - V_{P\Sigma}$ decreases for pnictogens lighter than Sb, we find ΔE_Σ to be at least 7 and 170 times smaller for As and P, respectively, than for Sb. We therefore expect that these lighter atoms could be magnetically trapped after buffer-gas cooling for long enough to remove the buffer gas, which may allow for observation of collisions between trapped pnictogen atoms.

Pnictogen atom-atom collisions could potentially be used as a path to the creation of ultracold pnictogen ensembles. The N–N system has been demonstrated to be sufficiently elastic that evaporative cooling can likely be achieved [10], with Zeeman relaxation driven primarily by the magnetic dipole-dipole interaction. With the same magnetic moment, P and possibly As may exhibit similar behavior. We note that the wavelengths of optical $E1$ transitions from the ground states of pnictogens lighter than Sb are lower than 200 nm [32], presenting a formidable challenge for laser cooling of these atoms. However, buffer-gas cooling has been used to produce ensembles of N, Sb, and Bi with over 10^{11} atoms [9,18], and similar performance is expected for the other pnictogens. The combination of buffer-gas cooling, magnetic trapping, and evaporative cooling may allow for studies and applications of ultracold N, P, and As.

ACKNOWLEDGMENTS

We are grateful to Roman Krems for use of his scattering code and for many helpful discussions. This work was supported by the NSF under Grant No. PHY-1067990 and through the Harvard-MIT Center for Ultracold Atoms, and by RFBR under Project No. 11-03-00081.

[1] A. A. Buchachenko, Y. V. Suleimanov, G. Chałasiński, and M. M. Szczęśniak, Phys. Scr. **80**, 048109 (2009).
[2] R. V. Krems and A. Dalgarno, Phys. Rev. A **68**, 013406 (2003).
[3] T. V. Tscherbul, A. A. Buchachenko, A. Dalgarno, M.-J. Lu, and J. D. Weinstein, Phys. Rev. A **80**, 040701 (2009).
[4] C. B. Connolly, Y. S. Au, E. Chae, T. V. Tscherbul, A. A. Buchachenko, Hsin-I. Lu, W. Ketterle, and J. M. Doyle, Phys. Rev. Lett. **110**, 173202 (2013).
[5] C. I. Hancox, S. C. Doret, M. T. Hummon, R. V. Krems, and J. M. Doyle, Phys. Rev. Lett. **94**, 013201 (2005).
[6] R. V. Krems, J. Kłos, M. F. Rode, M. M. Szczęśniak, G. Chałasiński, and A. Dalgarno, Phys. Rev. Lett. **94**, 013202 (2005).
[7] C. I. Hancox, S. C. Doret, M. T. Hummon, L. Luo, and J. M. Doyle, Nature (London) **431**, 281 (2004).
[8] A. A. Buchachenko, G. Chałasiński, M. M. Szczęśniak, and R. V. Krems, Phys. Rev. A **74**, 022705 (2006).
[9] S. E. Maxwell, M. T. Hummon, Y. Wang, A. A. Buchachenko, R. V. Krems, and J. M. Doyle, Phys. Rev. A **78**, 042706 (2008).

[10] T. V. Tscherbul, J. Kłos, A. Dalgarno, B. Zygelman, Z. Pavlovic, M. T. Hummon, H.-I. Lu, E. Tsikata, and J. M. Doyle, Phys. Rev. A **82**, 042718 (2010).
[11] M. T. Hummon, T. V. Tscherbul, J. Kłos, Hsin-I. Lu, E. Tsikata, W. C. Campbell, A. Dalgarno, and J. M. Doyle, Phys. Rev. Lett. **106**, 053201 (2011).
[12] P. S. Żuchowski and J. M. Hutson, Phys. Chem. Chem. Phys. **13**, 3669 (2011).
[13] J. Kłos, J. Chem. Phys. **123**, 024308 (2005).
[14] X. Chu, A. Dalgarno, and G. C. Groenenboom, Phys. Rev. A **72**, 032703 (2005).
[15] A. A. Buchachenko, M. M. Szczęśniak, and G. Chałasiński, J. Chem. Phys. **124**, 114301 (2006).
[16] X. Chu, A. Dalgarno, and G. C. Groenenboom, Phys. Rev. A **75**, 032723 (2007).
[17] A. A. Buchachenko, Proc. R. Soc. A **467**, 1310 (2011).
[18] M. T. Hummon, W. C. Campbell, Hsin-I. Lu, E. Tsikata, Y. Wang, and J. M. Doyle, Phys. Rev. A **78**, 050702(R) (2008).
[19] C. Johnson, B. Newman, N. Brahms, J. M. Doyle, D. Kleppner, and T. J. Greytak, Phys. Rev. A **81**, 062706 (2010).
[20] J. B. Hasted, *Physics of Atomic Collisions* (American Elsevier, New York, 1972).
[21] N. Brahms, T. V. Tscherbul, P. Zhang, J. Kłos, R. C. Forrey, Y. S. Au, H. R. Sadeghpour, A. Dalgarno, J. M. Doyle, and T. G. Walker, Phys. Chem. Chem. Phys. **13**, 19125 (2011).
[22] H.-J. Werner and P. J. Knowles, J. Chem. Phys. **89**, 5803 (1988).
[23] H.-J. Werner and P. J. Knowles, J. Chem. Phys. **82**, 5053 (1985).
[24] P. J. Knowles and H.-J. Werner, Chem. Phys. Lett. **115**, 259 (1985).
[25] B. Metz, H. Stoll, and M. Dolg, J. Chem. Phys. **113**, 2563 (2000).
[26] K. A. Peterson, J. Chem. Phys. **119**, 11099 (2003).
[27] D. E. Woon and J. T. H. Dunning, J. Chem. Phys. **100**, 2975 (1994).
[28] J. D. Watts, J. Gauss, and R. J. Bartlett, J. Chem. Phys. **98**, 8718 (1993).
[29] P. J. Knowles, C. Hampel, and H.-J. Werner, J. Chem. Phys. **99**, 5219 (1993).
[30] S. F. Boys and F. Bernardi, Mol. Phys. **19**, 553 (1970).
[31] S. M. Cybulski and R. R. Toczyłowski, J. Chem. Phys. **111**, 10520 (1999).
[32] A. Kramida, Y. Ralchenko, J. Reader, and NIST ASD Team (2012), *NIST Atomic Spectra Database (version 5.0)*, [Online], URL http://physics.nist.gov/asd.